Astronomy & Astrophysics manuscript no. 0404reip
April 28, 2009

Suzaku measurement of Abell 2204's intracluster gas temperature profile out to 1800 kpc.
(Research Note)

T. H. Reiprich[1], D. S. Hudson[1], Y.-Y. Zhang[1], K. Sato[2], Y. Ishisaki[3], A. Hoshino[3], T. Ohashi[3], N. Ota[4,5], and Y. Fujita[6]

[1] Argelander Institute for Astronomy, Bonn University, Auf dem Hügel 71, D-53121 Bonn, Germany
e-mail: `thomas@reiprich.net`
[2] Graduate School of Natural Science and Technology, Kanazawa University, Kakuma, Kanazawa, Ishikawa, 920-1192, Japan
[3] Department of Physics, Tokyo Metropolitan University, 1-1 Minami-Osawa, Hachioji, Tokyo 192-0397, Japan
[4] Institute of Space and Astronautical Science (ISAS/JAXA), 3-1-1 Yoshinodai, Sagamihara, Kanagawa 229-8510, Japan
[5] Max-Planck-Institut für extraterrestrische Physik, 85748 Garching, Germany
[6] Department of Earth and Space Science, Graduate School of Science, Osaka University, Toyonaka, Osaka 560-0043, Japan

Received 2008

ABSTRACT

Context. Measurements of intracluster gas temperatures out to large radii, where much of the galaxy cluster mass resides, are important for using clusters for precision cosmology and for studies of cluster physics. Previous attempts to measure robust temperatures at cluster virial radii have failed.

Aims. The goal of this work is to measure the temperature profile of the very relaxed symmetric galaxy cluster Abell 2204 out to large radii, possibly reaching the virial radius.

Methods. Taking advantage of its low particle background due to its low-Earth orbit, *Suzaku* data are used to measure the outer temperature profile of Abell 2204. These data are combined with *Chandra* and *XMM-Newton* data of the same cluster to make the connection to the inner regions, unresolved by *Suzaku*, and to determine the smearing due to *Suzaku*'s point spread function.

Results. The temperature profile of Abell 2204 is determined from ~10 kpc to ~1800 kpc, close to an estimate of r_{200} (the approximation to the virial radius). The temperature rises steeply from below 4 keV in the very center up to more than 8 keV in the intermediate range and then decreases again to about 4 keV at the largest radii. Varying the measured particle background normalization artificially by ±10% does not change the results significantly. Several additional systematic effects are quantified, e.g., those due to the point spread function and astrophysical fore- and backgrounds. Predictions for outer temperature profiles based on hydrodynamic simulations show good agreement. In particular, we find the observed temperature profile to be slightly steeper but consistent with a drop of a factor of 0.6 from 0.3 r_{200} to r_{200}, as predicted by simulations.

Conclusions. Intracluster gas temperature measurements up to r_{200} seem feasible with *Suzaku*, after a careful analysis of the different background components and the effects of the point spread function. Such measurements now need to be performed for a statistical sample of clusters. The result obtained here indicates that numerical simulations capture the intracluster gas physics well in cluster outskirts.

Key words. X-rays: galaxies: clusters – galaxies: clusters: individuals: Abell 2204

1. Introduction

Cosmologically, the most important parameter of galaxy clusters is their total gravitational mass. X-rays offer an attractive way to determine this mass through measurements of the intracluster gas temperature and density structures. X-rays are also a unique tool to study the physics of the hot cluster gas; e.g., gas temperature profiles allow constraints on (the suppression of) heat conduction. Consequently, constraining cluster temperature profiles has been the subject of many (partially contradictory) works in the recent past (e.g., Markevitch et al. 1996; Fukazawa 1997; Markevitch et al. 1998; Irwin et al. 1999; White 2000; Irwin & Bregman 2000; Allen et al. 2001; De Grandi & Molendi 2002; Zhang et al. 2004; Vikhlinin et al. 2005; Arnaud et al. 2005; Kotov & Vikhlinin 2005; Piffaretti et al. 2005; Hudson & Reiprich 2007; Pratt et al. 2007; Snowden et al. 2008; Leccardi & Molendi 2008).

Unfortunately, making these measurements is quite challenging in outer cluster regions. Even with *XMM-Newton* and *Chandra*, it is very difficult to determine temperature profiles reliably out to more than about 1/2 the cluster virial radius, $r_{\rm vir}$ (see the references above but also Solovyeva et al. 2007, for a different view). As a result, only about 1/8 of the cluster volume is actually probed. The primary reason is not an insufficient collecting area or spectral resolution of current instruments: the limiting factor is the high particle background. Here, the X-ray CCDs onboard *Suzaku* come into play. Owing to its low-Earth orbit and short focal length, the background is much lower and more stable than for *Chandra* and *XMM-Newton* (Mitsuda et al. 2007), making *Suzaku* a very promising instrument for finally settling the cluster temperature profile debate. And indeed, some of us have recently succeeded in measuring the temperature and metal abundance in the outskirts of the merging clusters A399/A401 (Fujita et al. 2008). Here, we go one step further and also confirm this great prospect for outer cluster regions whose emissivity is

---

Send offprint requests to: T.H. Reiprich not enhanced by merging activity and determine the temperature profile of the regular cluster Abell 2204 out to ∼1800 kpc with *Suzaku*. This radius is close to an estimate of r_{200}; i.e., the radius within which the mean total density equals 200 times the critical density, often used as approximation to the virial radius. Note that shortly after this paper was submitted, another study of a cluster temperature profile towards very large radii with *Suzaku* was submitted by George et al. (2008).

Throughout, we assume $\Omega_{\rm m} = 0.3$, $\Omega_\Lambda = 0.7$, and $H_0 = 71$ km/s/Mpc; i.e., at the redshift of Abell 2204 ($z = 0.1523$), 1' = 157 kpc.

2. Observations, Reduction, Analysis

2.1. *Chandra* and *XMM-Newton* data

Abell 2204 was analyzed with *Chandra* as part of the *HIFLUGCS* (Reiprich & Böhringer 2002) follow-up. The reduction and analysis are similar to those outlined in Hudson et al. (2006). The total clean exposure of the two archival observations is 18.6 ks. Further details are described in Hudson et al. (2009).

The *XMM-Newton* analysis of Abell 2204 is published (Zhang et al. 2008). Extrapolating the mass profile using the published gas density and temperature profile, we found $r_{200} = 11.75' = 1840$ kpc.

2.2. *Suzaku* data

Abell 2204 was observed with *Suzaku* on September 17–18, 2006. We started from the cleaned event files (processing version 1.2.2.3) and reran the ftools xisputpixelquality and xispi, using HEAsoft 6.2 and CALDB 070409. Using xselect, the event files were further filtered by applying the criteria STATUS=0:65535, COR>6, and ELV>10. The good exposure amounts to about 50 ks for each of the four XIS using both 3x3 and 5x5 editing modes. Figure 1 (left) shows the combined image and the regions selected for spectral analysis.

The widths of the annuli were chosen to be about twice as large as the half power diameter of the point spread function (PSF). Combined spectra were extracted using the filtered 3x3 and 5x5 editing mode events files. Using four regions from each of the four detectors, this resulted in 16 spectra total from the source observation. The spectra were grouped to have at least 50 counts in each energy channel.

We checked the spectra for contamination by solar wind charge exchange emission. The ACE SWEPAM proton flux was less than 6×10^8 protons/s/cm^2 during the observation. Therefore, no strong flaring is expected (Fujimoto et al. 2007). Moreover, we checked the soft band (<2 keV) XIS-1 lightcurve of the local background region and did not find any indication of flaring.

Response files were created with xisrmfgen and xissimarfgen. We generated the first Ancillary Response File (ARF) by feeding an image, constructed from the double β model fit to the *Chandra* surface brightness profile, into xissimarfgen. This ARF was later used to model the cluster emission. For the second ARF, which was used when modeling the Galactic fore- and cosmic X-ray background, we assumed a uniform photon distribution. We simulated 10^7 photons per detector using medium sampling.

Night Earth data were used to create spectra of the particle background for each region and each detector, weighting the spectra by cutoff rigidity.[1] These particle spectra were supplied as background spectra to the XSPEC (version 12.3.1) fitting routine. The cluster emission was modeled with an absorbed thermal model (phabs*apec). The cosmic X-ray background and Galactic emission were accounted for with an absorbed powerlaw and an unabsorbed thermal model, respectively (phabs*pow+apec).

All 16 spectra were fitted simultaneously. We froze the hydrogen column density at 6.07×10^{20} cm^{-2} (Kalberla et al. 2005), the cluster redshift at $z = 0.1523$ (Struble & Rood 1987), the redshift and metal abundance of the Galactic component at $z = 0$ and $A = 1$ solar, and the powerlaw photon index at 1.41 (Kushino et al. 2002). The remaining parameters of the fore- and background components were left free and linked across all regions and detectors. The temperatures, metallicities (Anders & Grevesse 1989), and normalizations of the cluster emission were left free and linked across the four detectors. Annulus 4 served to help constrain the fore- and background components because no significant "contaminating" cluster emission is expected beyond the estimated r_{200}, so the normalization of the thermal cluster model was frozen at 0 in this annulus.

In the spectral fitting for this hot cluster, we ignored all photons with energies $\leq$0.7 keV. We did this to minimize any systematic uncertainties due to the correction for the effective area degradation by the contamination, due to the Galactic foreground subtraction, and due to the influence of possible low intensity solar wind charge exchange emission. The upper energy cut used for the fitting was set at 10 keV (8 keV for XIS-1, due to remaining calibration uncertainties). The Si K edge (1.8–1.9 keV) and, for XIS-0, the calibration Mn K line (5.7–6.0 keV) were excluded. The range 7.2–8.0 keV was ignored because of the presence of the strong instrumental Ni K line. Overall, the model provided a good description of the data, resulting in $\chi^2_{\rm red} = 1.20$ for 4097 degrees of freedom.

3. Results

The spectra and best fit models are shown in Figure 2. In the left panel, we show all 16 spectra (data points with errors) and corresponding best fit models (solid lines). The particle background was subtracted from the data points. Each spectrum has three model lines, one thin line representing the cluster emission, another thin line representing the combined Galactic fore- and cosmic X-ray background, and the thick line the sum of these (i.e., the thick lines should match the data points). The main purpose of this plot is to show that there are no strong residuals anywhere.

In the right panel, we show the same plot for the most important region (bin 3). It is instructive to compare the role of the different fore- and background components relative to the cluster emission. Therefore, we show here also the particle background spectra as stars with thick error bars (which were subtracted from the data) as well as the Galactic fore- and cosmic X-ray background components individually. For clarity, let's focus on the XIS1 spectra; i.e., the red data points and lines. The thick line matches the data points pretty well, as it should. Now let's start at the low energies: The uppermost thin line represents the Galactic foreground component. This component dominates over all other components up to about 1 keV. The next line represents the cluster component, which starts to dominate (marginally) around 1 keV until the cosmic X-ray background

---

[1] See http://www.astro.isas.jaxa.jp/suzaku/analysis/xis/nte/ for details. Additionally, we discarded a very small fraction of events by requiring T_SAA_HXD>436, resulting in 795 ks total exposure time.

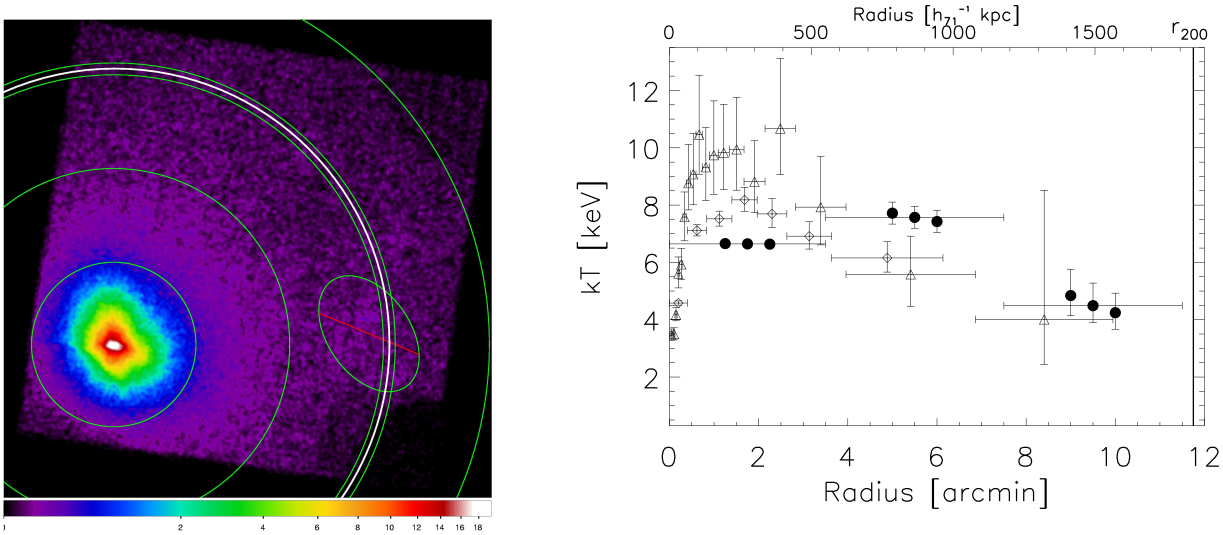

Fig. 1. *Left panel*: *Suzaku* image of A2204 combining all four XIS detectors. Also indicated are the regions used for the spectral analysis (green) and the estimated r_{200} (white). The outermost annulus (annulus 4, beyond r_{200}) was used to aid in the local fore- and background estimation. The elliptical region contains emission from unrelated sources and was excluded from the spectral analysis. *Right panel*: Gas temperatures as function of radius as measured with *Suzaku* (filled circles), *XMM-Newton* (diamonds), and *Chandra* (triangles). For each *Suzaku* bin three temperatures are shown. The upper and lower temperature values were obtained by artificially decreasing and increasing the particle background normalization by 10%, respectively. The bins are slightly offset in this plot for clarity. All errors are given at the 90% confidence level.

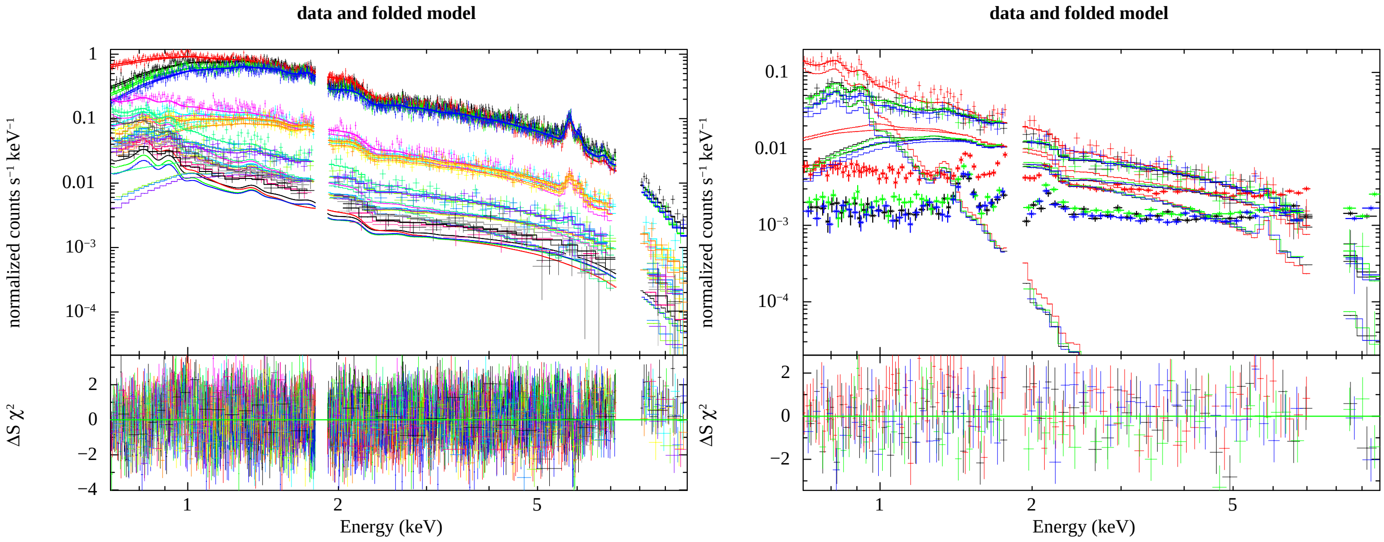

Fig. 2. *Left panel*: Particle background subtracted *Suzaku* spectra from all four regions (innermost region at the top, outermost region at the bottom) and from all four detectors (e.g., for the innermost region: black: XIS0, red: XIS1, green: XIS2, blue: XIS3). Also shown are the models (total, cluster, and combined Galactic fore- and cosmic X-ray background) from the simultaneous fit as well as the residuals in terms of standard deviations. There are no strong systematic deviations for any of the regions or detectors. *Right panel*: Same as left but only for bin 3 (7.5′–11.5′). In this plot the Galactic fore- and cosmic X-ray background models are shown separately, and the subtracted particle background is also given (by the thicker data points at the bottom). The cluster emission dominates over the other components only in the range ∼1–1.5 keV and even there only marginally (see text).

becomes stronger around 1.5 keV. The particle background starts to dominate over the Galactic foreground around 1.4 keV, over the cluster component around 3 keV, and over the cosmic X-ray background between 4 and 5 keV. This plot illustrates that a cluster temperature determination in this region requires long exposures and is getting close to the limit of *Suzaku*'s capabilities. In case of *Chandra* or *XMM-Newton*, the particle background would start to dominate over each of the other components at much lower energies. The same plot for bin 4 looks quite similar, there are just fewer data points and no cluster emission.

Figure 1 (right) shows projected gas temperature profiles measured with *Chandra*, *XMM-Newton*, and *Suzaku*. In the innermost region ($\lesssim 0.4'$) the *XMM-Newton* temperature is consistent with the range of best fit temperatures obtained with *Chandra* (3.5–7.6 keV). In the region ∼1–2′, however, *Chandra* gives systematically higher temperatures than *XMM-Newton*. The primary reasons for this are, first, that the *XMM-Newton* profile is not corrected for PSF smearing, so the temperatures in this region are slightly underestimated; and, second, that the *Chandra* effective area calibration is, apparently, inaccurate, resulting in overestimates of the temperature at high temperatures

Table 1. Best fit *Suzaku* cluster temperatures, metallicities, and the corresponding statistical uncertainties (90% confidence level) of the four radial bins.

Bin	Radius/[$'$]	Radius/[R_{200}]	$kT_{\rm X}$/[keV]	A/[solar]
1	0–3.5	0–0.30	$6.65^{+0.08}_{-0.08}$	$0.43^{+0.02}_{-0.02}$
2	3.5–7.5	0.30–0.64	$7.57^{+0.39}_{-0.38}$	$0.37^{+0.07}_{-0.07}$
3	7.5–11.5	0.64–0.98	$4.49^{+0.79}_{-0.59}$	$0.25^{+0.25}_{-0.22}$
4	12–16	1.02–1.36	–	–

(e.g., Snowden et al. 2008; Sun et al. 2008, and L. David's presentation[2]). The central *Chandra* temperatures determined here are consistent with those from Sanders et al. (2005). In the region ∼3–6$'$ *Chandra* and *XMM-Newton* give consistent results.

The *Suzaku* best fit temperatures and uncertainties are given in Tab. 1. The innermost *Suzaku* bin covers $0'$–$3.5'$ and, obviously, contains emission from quite a range of temperatures. The result of the single temperature fit ($6.65^{+0.08}_{-0.08}$ keV) lies roughly in the middle of this temperature range, as expected. The *Suzaku* best fit temperature in the second bin ($3.5'$–$7.5'$, $7.57^{+0.39}_{-0.38}$ keV) is slightly higher compared to the *Chandra* and *XMM-Newton* temperatures. The primary reason for this is most likely contamination from emission from the very bright region $<3.5'$ due to *Suzaku*'s PSF (contamination is ∼50%, see discussion below). Even though A2204 appears quite regular on large scales (e.g., Schuecker et al. 2001), possible deviations from exact spherical symmetry of the temperature structure may also introduce some scatter in the comparisons.

For the purpose of this paper, bin 3 covers the most important region. It extends from $7.5'$ to $11.5'$; i.e., from 64% to 98% of the estimated r_{200}. The *Suzaku* best fit temperature ($4.49^{+0.79}_{-0.59}$ keV) is significantly lower than the temperatures measured further in. For *Chandra* and *XMM-Newton*, temperature measurements in the low surface brightness cluster outskirts are strongly affected by the uncertainty in the particle background. We tested the influence of the particle background on the *Suzaku* results by artificially changing the normalization of the Night Earth spectra by a very conservative (e.g., Tawa et al. 2008) ±10% and repeating the fitting procedure. We found that the new best fit temperatures are consistent with the statistical uncertainty of the standard fit (Fig. 1). This demonstrates that the results obtained here are not affected significantly by uncertainties in the particle background subtraction.

We also attempted a temperature measurement with *Chandra* in the region 6.9–9.9$'$. The *Chandra* best fit temperature is consistent with the allowed *Suzaku* temperature range but the statistical uncertainty (excluding systematic effects due to the particle background) is too large for a meaningful constraint of the temperature with *Chandra*.

4. Discussion

We showed clear evidence that the temperature of this relaxed cluster declines significantly when going from the inner to the outer regions. This is expected theoretically (e.g., Frenk et al. 1999). To compare, in detail, the result obtained here to predictions, we overplotted in Fig. 3 (left) the average temperature profile in cluster outskirts as determined with hydrodynamical simulations of massive clusters by Roncarelli et al. (2006, Sample A in their Tab. 2). These authors specifically studied the regions around the virial radius. Note that magnetic fields and cosmic rays were not included in their simulations. For the comparison, we used $r_{200} = 11.75'$ and $kT_{\rm X}(0.3r_{200}) = 7.42$ keV. The latter was calculated by taking the average of the best fit *Chandra* and *XMM-Newton* temperatures of the bins that include $0.3r_{200}$ (shown in Fig. 3, left). We excluded the *Suzaku* measurement because its broad PSF makes an accurate determination at this radius difficult.

The temperature of the inner *Suzaku* bin shown is slightly higher but consistent with the prediction (keep in mind that, in general, regions left of bin centers carry more weight in the temperature determination than regions right of bin centers, because the surface brightness decreases rapidly with radius). As mentioned above and discussed in more detail below, this bin is strongly affected by PSF smearing, so the actual projected temperature may be lower. Due to the steep surface brightness profile, deprojection would likely result in only a minor increase of the temperature estimate. The important outer bin is much less affected by PSF and projection effects and is slightly lower but consistent with the prediction. In conclusion, the observed outer temperature profile is slightly steeper but consistent with a drop of a factor of 0.6 from 0.3 r_{200} to r_{200}, as predicted by simulations.

We tested illustratively what the improvement in the uncertainty of a total mass estimate is due to the improvement of the uncertainty of the temperature profile provided by the *Suzaku* data. We fitted powerlaws to the outermost *XMM-Newton* data point and the *Chandra* and *Suzaku* outermost data points, respectively, taking into account the upper and lower statistical (90%) errors of the latter two. Then we determined a fiducial total mass using the best fit single β model parameters for the density profile (from Reiprich & Böhringer 2002) and the powerlaw model parameters for the temperature profiles, under the assumption of hydrostatic equilibrium. Using the *Chandra* temperature we found $M(<1840\,{\rm kpc}) = 5.34^{+2.97}_{-2.10} \times 10^{14} M_{\odot}$. Using *Suzaku* we found $M(<1840\,{\rm kpc}) = 6.18^{+0.64}_{-0.56} \times 10^{14} M_{\odot}$; i.e., the uncertainty due to the temperature profile decreased from 40–60% (*Chandra*) to 10% (*Suzaku*). So, this represents a significant improvement of a factor of ∼5 (factor of ∼3 when taking into account the different exposure times). Note that a full analysis of the total mass profile will be performed in a more in-depth work.

In the following, we discuss and quantify several systematic effects. We discuss these issues here at some length because this is one of the first papers determining cluster properties out to r_{200}, where the surface brightness is very low and systematic effects potentially quite important. In summary, we found that the combination of all quantified systematic effects is of the same order as the statistical uncertainty in the most relevant bin ($7.5'$–$11.5'$). The individual results of the tests are summarized in Tab. 2.

We start with the particle background. The reproducibility of this background component for *Suzaku* is better than about 3% (e.g., Tawa et al. 2008). Here, we conservatively assumed 5% and found best fit temperatures and errors for the third bin as $4.66^{+0.81}_{-0.65}$ keV and $4.32^{+0.77}_{-0.54}$ keV. So, for *Suzaku*, this effect is very small.

Next, we discuss the influence of *Suzaku*'s PSF. We performed ray tracing simulations using the xissim tool (Ishisaki et al. 2007) using 10^7 photons per energy and detector. We assumed Abell 2204's surface brightness profile to follow the best double β model fit to the *Chandra* data. We followed a procedure very similar to the one described by Sato et al. (2007) and

---

[2] http://cxc.harvard.edu/ccw/proceedings/07_proc/presentations/david/

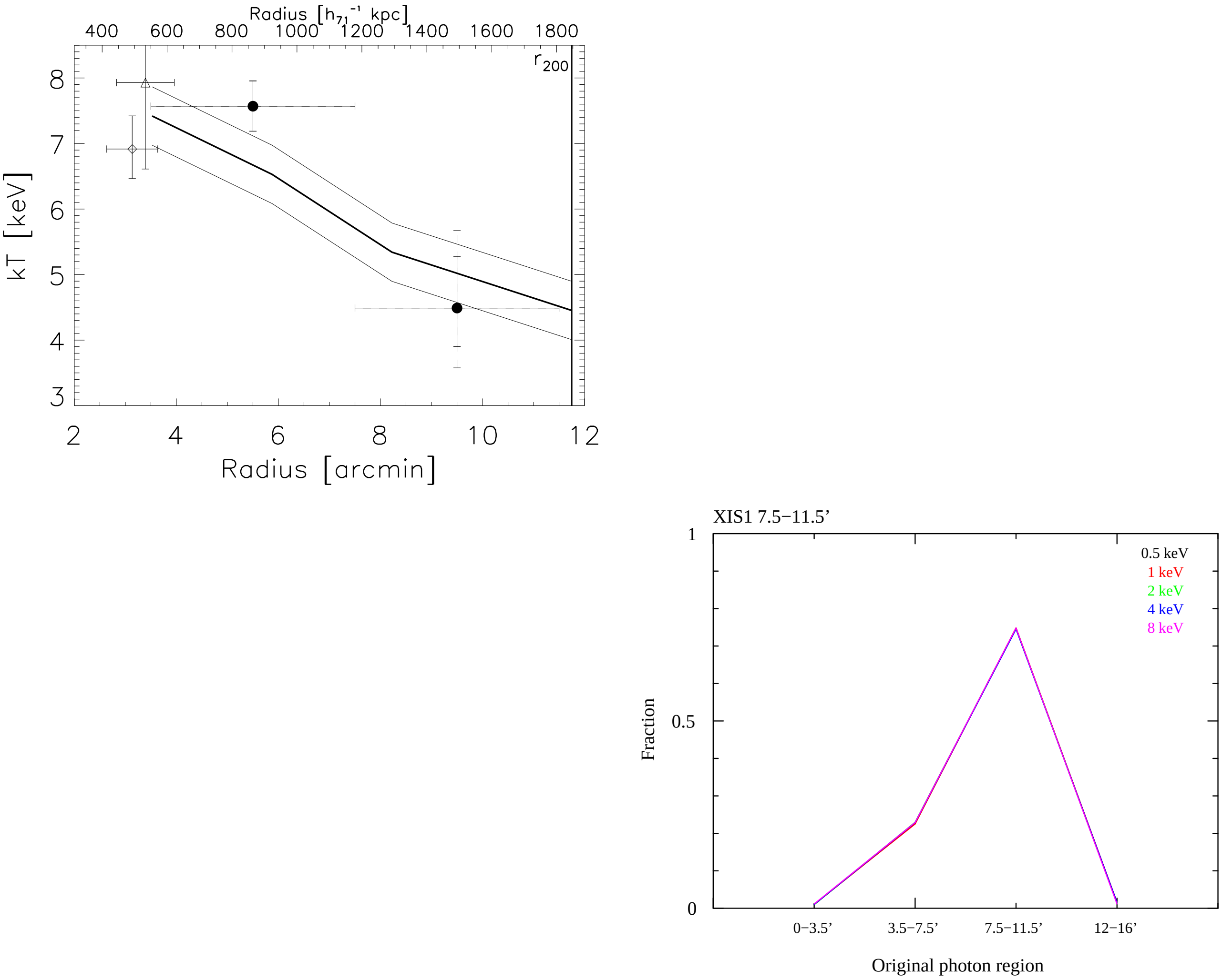

Fig. 3. *Left panel:* Observed outer temperature profile compared to profile and scatter predicted by hydrodynamical simulations of Roncarelli et al. (2006, solid lines). Symbols have the same meaning as in Fig. 1. For clarity, only the two *Chandra* and *XMM-Newton* data points are shown that were used to determine $kT_X(0.3r_{200})$. The other *Chandra* and *XMM-Newton* data points further out are consistent with the simulation results. The dashed error bars of the outer *Suzaku* bin indicate the combined statistical plus systematic error range, calculated as described in the text and using the uncertainties given in Tab. 2. *Right panel:* Contamination fractions of the XIS1 bin 7.5′–11.5′ determined from ray tracing simulations. 75% of the photons detected in this bin also originated in this region. The energy dependence is negligible (the lines for all five energies overlap) and the results are very similar for the other detectors.

Table 2. Systematic uncertainties of the cluster temperature measurement in the bin 7.5′–11.5′.

Test	ΔkT_X/[keV]
1 Particle background (−5%)	+0.18
2 Particle background (+5%)	−0.17
3 PSF (25% contamination)	−0.68
4 Foreground modeling (double thermal)	+0.61
5 ROSAT foreground (thermal)	+0.32
6 ROSAT background (powerlaw)	+0.46
7 ARF from ROSAT surface brightness	+0.01
8 Extrapolated cluster emission beyond r_{200}	+0.24

found that the second bin (3.5′–7.5′) is significantly (49%) contaminated by emission originating in the cluster center (<3.5′). The most important region, the third bin (7.5′–11.5′) is contaminated by 25%; i.e., a relatively small fraction (see Fig. 3, right, for the contamination fractions of this bin determined for XIS1, as a representative example). The energy and detector dependence of the PSF were found to be small enough to be negligible here. The same is true for the fine details of the model for the surface brightness profile, since we found very similar fractions when repeating this analysis using the best fit double β model as obtained from *ROSAT PSPC* pointed data.

Naively, one could assume that a simple PSF contamination correction could be performed, starting with the assumption that 49% of the emission in the 3.5′–7.5′ bin comes from a plasma at kT_X = 6.65 keV (Tab. 1). However, this would not be accurate, as the *Chandra* and *XMM-Newton* data reveal a wide range of temperatures at different distances from the cluster center (Fig. 1). A detailed correction for the PSF effects, therefore, requires a large number of ray tracing simulations to be performed, using fine *Chandra* temperature bins, to determine precisely how much emission from plasma at what temperature contaminates each of the *Suzaku* bins. A detailed correction for the PSF effects is beyond the scope of this paper. Such a correction will be performed in a more in-depth analysis, using the longer *Chandra* observation of this cluster (Sanders et al. 2009) and the recently updated effective area calibration. Here, we follow a rather conservative route and quantify the changes in temperature and uncertainty by assuming the temperature for the emission, contaminating the important third bin, to lie in the range 6.0–8.0 keV. Furthermore, we freeze the metallicities of the third bin to 0.2 and that of the contaminating emission to 0.3. This results in the following best fit temperatures and uncertainties: $kT_{\rm X}(7.5'–11.5') = 4.13^{+0.96}_{-0.77}$ keV (for $kT_{\rm contami} = 6$ keV) and $kT_{\rm X}(7.5'–11.5') = 3.81^{+0.90}_{-0.67}$ keV (for $kT_{\rm contami} = 8$ keV). Changing the metallicities of the third bin to 0.15 and 0.25 has a quite negligible influence on the best fit temperatures. The same is true when changing the metallicity from the contaminating emission from the second bin to 0.25 and 0.35. In Tab. 2 and the calculation of the total systematic uncertainty we use the more conservative ($kT_{\rm contami} = 8$ keV) result.

We specifically designed the *Suzaku* observation in such a way as to have a cluster free region available to help constrain Galactic fore- and cosmic X-ray background directly and locally, using the same observation. This ensures that the results are not affected by systematic calibration differences between different satellites and varying point source subtraction fractions. Still, we checked whether the resulting parameter values are in a reasonable range. We found that the normalization of the powerlaw component expected from deep CXB studies using several different satellites is lower by factors 0.77–0.62 compared to our best fit normalization. We then froze the powerlaw normalization to the highest (Vecchi et al. 1999) and lowest (Revnivtsev et al. 2003) normalization we found in the literature, resulting in temperatures $6.08^{+0.98}_{-0.82}$ and $6.84^{+1.17}_{-0.72}$ keV, respectively, in the third bin. This procedure results in worse fits but note that, in the latter case, the temperature is significantly hotter than when leaving the powerlaw normalization free. Since intensity variations of the CXB may be correlated with large scale structure, we decided to use the independent *ROSAT PSPC* observation of Abell 2204 and fitted the same fore-/background model in the energy band 0.3–2.4 keV to the outskirts. We found that the normalization is fully consistent (factor 0.81–1.04) with the higher powerlaw normalization from the *Suzaku* data of Abell 2204. Moreover, we also found the temperature and normalization of the thermal component to be fully consistent with the *Suzaku* results. In particular, for the Galactic emission, we found temperatures of $0.25^{+0.02}_{-0.01}$ keV (*Suzaku*) and $0.26^{+0.01}_{-0.01}$ keV (*ROSAT*), quite typical of this foreground component; i.e., there was no indication of significant hot cluster or accretion shock emission "contaminating" annulus 4. We, therefore, conclude that our Galactic fore- and cosmic X-ray background modeling is adequate.

Recall that the purely statistical uncertainties on these fore- and background components are already included in our quoted statistical errors on the cluster temperatures because in our standard analysis we performed a simultaneous fit of all the astrophysical fore- and background components together with the cluster component; i.e, the relevant parameters for these models were all free to vary. For the calculation of the total systematic uncertainty, we additionally included effects, which relate to the modeling of the Galactic thermal emission as well as the spatial variation of the fore- and background components, as described in the following.

Several authors used more than one spectral component to model the Galactic foreground emission (e.g., Sato et al. 2007; Snowden et al. 2008; Henley & Shelton 2008). Therefore, we tried a two component foreground model (phabs*apec+apec) instead of a single component model (apec) for the Suzaku observation. As best fit temperatures for the Galactic components we found 0.28 keV for the absorbed component and 0.13 keV for the unabsorbed one, in good agreement with the typical values quoted by Snowden et al. (2008). Furthermore, the new powerlaw model normalization (representing the unresolved cosmic X-ray background) is only 2.5% lower than in the original fit. This change is much smaller than the statistical error on this normalization.

We found that the resulting new best fit cluster temperature in the most important and most affected third bin (7.5′–11.5′) gets a bit higher but not significantly so (5.10 keV). On the one hand, this lends confidence to our approach; on the other hand, this result is also not too surprising since in our spectral analysis we ignored all photons with energies E<0.7 keV, so the cluster temperature measurements are by construction less sensitive to uncertainties in the soft fore- and background.

Also, $\chi^2_{\rm red}$ does not change by adding this additional model component, showing that no significant improvement can be achieved by adding this second thermal component for the data under consideration here.

Moreover, the relative statistical uncertainties stay very similar, e.g., for the best fit cluster temperature in the third bin the errors at the 90% confidence level are −13% +18% (single thermal Galactic foreground model) and −15% +21% (double thermal Galactic foreground model); therefore, the simple single thermal model does not result in a significant underestimate of statistical errors. In our systematic error analysis we do include the model dependence in the final error.

Last not least, we tested the double thermal model in the *ROSAT* analysis of the foreground emission. We found very similar best fit temperatures for the Galactic components (absorbed 0.25 keV, unabsorbed 0.13 keV), although *ROSAT*'s poor energy resolution results in significantly enlarged errors for the temperatures of the two thermal components (the two temperature ranges overlap; degeneracies cannot be broken, resulting in an unstable error analysis). The change in the powerlaw normalization is again well within the statistical uncertainty.

Next, we tested the influence of a possible spatial variation of the fore- and background estimates. The regions selected for the fore- and background analysis in the *ROSAT* observation differ from those in the *Suzaku* observation. Therefore, we refit the *Suzaku* data but this time not letting the powerlaw and thermal component vary freely but, separately, freezing them to the values determined from the *ROSAT* observation (after correction for the different covered areas). The best fit cluster temperatures for the third bin do not change significantly. They are $4.81^{+0.81}_{-0.65}$ keV (foreground apec model frozen) and $4.95^{+0.85}_{-0.66}$ keV (background powerlaw model frozen). Both effects are included in the total systematic error analysis.

The Monte Carlo ARF calculation using xissimarfgen requires a priory knowledge of the cluster surface brightness distribution, which we provided using a double β model fit to the surface brightness measured with *Chandra*. We tested the influence of deviations from this assumed distribution on the cluster temperature measurements by instead generating ARFs using the best fit double β model from the *ROSAT* observation. The resulting best fit temperature in the third bin was almost unchanged (4.50 keV).

We assumed that the "cluster free" region (the forth bin) contains negligible cluster emission and argued that the best fit temperature for the Galactic foreground emission we found supports this assumption. Nevertheless, we performed an additional test to estimate the contribution of this assumption to the total systematic error. To this end, we determined a rough surface brightness profile using bins 1 through 3 and extrapolated it by conservatively assuming the surface brightness to drop by a factor of 5 from bin 3 to bin 4. Furthermore, we assumed a temperature of 2 keV and a metallicity of 0.2 solar in bin 4. We then included this cluster component in the model for bin 4, in addition to the fore- and background components, and redid the full simultaneous fit. The resulting new best fit cluster temperature in bin 3 is 4.73 keV; i.e., slightly higher than the original fit result but not significantly so. This rather small change is expected because the extrapolated surface brightness of this fourth bin is much lower than the surface brightness of the powerlaw background component. Therefore, the new normalization of the powerlaw background component is also only slightly lower (7%) compared to the original one. A detailed determination and discussion of the surface brightness profile and especially its error will be presented in a subsequent paper. We do add the effect of the possible cluster emission in bin 4 to the systematic error budget.

Some of the systematic effects described above raise the temperature (e.g., using a double thermal model for the Galactic foreground emission) others lower it (e.g., roughly accounting for PSF effects). To estimate the total systematic error as well as the combined statistical plus systematic error, we used the following scheme. We separately added all positive and negative errors from Tab. 2 in quadrature, resulting in a total systematic error $^{+0.88}_{-0.70}$ keV. The total systematic error is, therefore, slightly larger but of the same order as the statistical uncertainty ($^{+0.79}_{-0.59}$ keV). Then, we added the systematic and statistical errors in quadrature, resulting in a combined statistical plus systematic error $^{+1.18}_{-0.91}$ keV (shown as dashed error bars in Fig. 3).

For the comparison to simulated temperature profiles, the uncertainty of r_{200} as estimated from the extrapolated *XMM-Newton* density and temperature profiles may be important. For instance, using a cluster mean temperature and the relation of Evrard et al. (1996) would result in a larger value for r_{200}. Also, Arnaud et al. (2005) determined $r_{200} = 2075$ kpc using the same *XMM-Newton* data, probably due to the flatter temperature profile they found. This would make the observed temperature drop even steeper in terms of r_{200}, potentially resulting in tension between observation and simulations. We will redetermine r_{200} from the cluster mass profile, taking advantage of the information on the outer temperature from *Suzaku* in the more in-depth analysis of this cluster. It is reassuring to note that further corroboration for the r_{200} estimate used here comes from the independent weak lensing analysis of this cluster (Clowe & Schneider 2002), yielding $r_{200} = 11.8'$, in perfect agreement with our estimate.

The confirmation of the predictions from hydrodynamical simulations for the gas physics in cluster outskirts indicated here rests on the analysis of a single cluster. What is required for a general confirmation is the analysis of a statistical sample of clusters. In the future, this can be performed with dedicated cluster observations accumulating rapidly in the *Suzaku* archive.

Acknowledgements. THR acknowledges the hospitality of Tokyo Metropolitan University. We thank T. Erben, G. Hasinger, O.-E. Nenestyan, and P. Schneider for help in the early stages of this work, M. Markevitch for comments on the paper, and M. Roncarelli for sending electronic data tables of simulated clusters. THR, DSH, YYZ acknowledge support by the Deutsche Forschungsgemeinschaft through Emmy Noether Research Grant RE 1462/2 and by the German BMBF through the Verbundforschung under grant no. 50 OR 0601. KS acknowledges support by the Ministry of Education, Culture, Sports, Science and Technology of Japan, Grant-in-Aid for Scientific Research No. 19840043. NO thanks the Alexander von Humboldt Foundation for support.

References

Allen, S. W., Schmidt, R. W., & Fabian, A. C. 2001, MNRAS, 328, L37

Anders, E. & Grevesse, N. 1989, Geochim. Cosmochim. Acta, 53, 197

Arnaud, M., Pointecouteau, E., & Pratt, G. W. 2005, A&A, 441, 893

Clowe, D. & Schneider, P. 2002, A&A, 395, 385

De Grandi, S. & Molendi, S. 2002, ApJ, 567, 163

Evrard, A. E., Metzler, C. A., & Navarro, J. F. 1996, ApJ, 469, 494

Frenk, C. S., White, S. D. M., Bode, P., et al. 1999, ApJ, 525, 554

Fujimoto, R., Mitsuda, K., Mccammon, D., et al. 2007, PASJ, 59, 133

Fujita, Y., Tawa, N., Hayashida, K., et al. 2008, PASJ, 60, S343

Fukazawa, Y. 1997, PhD thesis, Univ. Tokyo

George, M. R., Fabian, A. C., Sanders, J. S., Young, A. J., & Russell, H. R. 2008, MNRAS, accepted. Preprint: arXiv:0807.1130, 807

Henley, D. B. & Shelton, R. L. 2008, ApJ, 676, 335

Hudson, D. S., Mittal, R., Reiprich, T. H., et al. 2009, A&A, submitted

Hudson, D. S. & Reiprich, T. H. 2007, in Heating vs. Cooling in Galaxies and Clusters of Galaxies, ed. H. Böhringer, G. W. Pratt, A. Finoguenov, & P. Schuecker (Berlin, Germany: ESO Astrophysics Symposia, Springer Verlag), 42–44

Hudson, D. S., Reiprich, T. H., Clarke, T. E., & Sarazin, C. L. 2006, A&A, 453, 433

Irwin, J. A. & Bregman, J. N. 2000, ApJ, 538, 543

Irwin, J. A., Bregman, J. N., & Evrard, A. E. 1999, ApJ, 519, 518

Ishisaki, Y., Maeda, Y., Fujimoto, R., et al. 2007, PASJ, 59, 113

Kalberla, P. M. W., Burton, W. B., Hartmann, D., et al. 2005, A&A, 440, 775, http://www.astro.uni-bonn.de/~webrai/english/tools_labsurvey.php

Kotov, O. & Vikhlinin, A. 2005, ApJ, 633, 781

Kushino, A., Ishisaki, Y., Morita, U., et al. 2002, PASJ, 54, 327

Leccardi, A. & Molendi, S. 2008, A&A, 486, 359

Markevitch, M., Forman, W. R., Sarazin, C. L., & Vikhlinin, A. 1998, ApJ, 503, 77

Markevitch, M., Mushotzky, R., Inoue, H., et al. 1996, ApJ, 456, 437

Mitsuda, K., Bautz, M., Inoue, H., et al. 2007, PASJ, 59, 1

Piffaretti, R., Jetzer, P., Kaastra, J. S., & Tamura, T. 2005, A&A, 433, 101

Pratt, G. W., Böhringer, H., Croston, J. H., et al. 2007, A&A, 461, 71

Reiprich, T. H. & Böhringer, H. 2002, ApJ, 567, 716

Revnivtsev, M., Gilfanov, M., Sunyaev, R., Jahoda, K., & Markwardt, C. 2003, A&A, 411, 329

Roncarelli, M., Ettori, S., Dolag, K., et al. 2006, MNRAS, 373, 1339

Sanders, J. S., Fabian, A. C., & Taylor, G. B. 2005, MNRAS, 356, 1022

Sanders, J. S., Fabian, A. C., & Taylor, G. B. 2009, MNRAS, 393, 71

Sato, K., Yamasaki, N. Y., Ishida, M., et al. 2007, PASJ, 59, 299

Schuecker, P., Böhringer, H., Reiprich, T. H., & Feretti, L. 2001, A&A, 378, 408

Snowden, S. L., Mushotzky, R. F., Kuntz, K. D., & Davis, D. S. 2008, A&A, 478, 615

Solovyeva, L., Anokhin, S., Sauvageot, J. L., Teyssier, R., & Neumann, D. 2007, A&A, 476, 63

Struble, M. F. & Rood, H. J. 1987, ApJS, 63, 543

Sun, M., Voit, G. M., Donahue, M., et al. 2008, ApJ, accepted. Preprint: arXiv:0805.2320, 805

Tawa, N., Hayashida, K., Nagai, M., et al. 2008, PASJ, 60, S11

Vecchi, A., Molendi, S., Guainazzi, M., Fiore, F., & Parmar, A. N. 1999, A&A, 349, L73

Vikhlinin, A., Markevitch, M., Murray, S. S., et al. 2005, ApJ, 628, 655

White, D. A. 2000, MNRAS, 312, 663

Zhang, Y.-Y., Finoguenov, A., Böhringer, H., et al. 2004, A&A, 413, 49

Zhang, Y.-Y., Finoguenov, A., Böhringer, H., et al. 2008, A&A, 482, 451